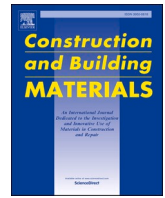




Contents lists available at ScienceDirect

# Construction and Building Materials

journal homepage: [www.elsevier.com/locate/conbuildmat](http://www.elsevier.com/locate/conbuildmat)

## Steel slag aggregate concrete filled-in FRP tubes: Volume expansion effect and axial compressive behaviour

Peng Feng<sup>a,\*</sup>, Zhiyuan Li<sup>a</sup>, Shanbao Zhang<sup>b</sup>, Jia-Qi Yang<sup>c</sup><sup>a</sup> MOE Key Lab of Civil Engineering Safety and Durability, Department of Civil Engineering, Tsinghua University, Beijing 100084, China<sup>b</sup> State Key Laboratory of Disaster Prevention & Mitigation of Explosion & Impact, Army Engineering University of PLA, Jiangsu, Nanjing 210007, China<sup>c</sup> School of Mechanics and Civil engineering, China University of Mining and Technology (Beijing), Beijing 100083, China

### ARTICLE INFO

#### Keywords:

Steel slag aggregate  
CFFT  
Volume expansion effect  
3D laser scanning  
Axial compressive behavior

### ABSTRACT

Using steel slag as concrete aggregate is an effective, eco-friendly method of steel slag disposal. However, the volume expansion of steel slag aggregates (SSAs) creates premature cracks and reduces the mechanical property and durability of concrete, limiting steel slag aggregate concrete (SSAC) applications. A concrete filled-in fiber-reinforced polymer (FRP) tube (CFFT) is a structural member that exploits the high tensile strength of FRP and the lateral expansion of concrete under compression. FRP tubes can be used for the external confinement of concrete to increase its strength and ductility. In this paper, a steel slag aggregate concrete filled-in FRP tube (SSACFFT) is proposed for steel slag disposal. The physical and mechanical properties of an SSACFFT were investigated experimentally. The volume changes in the SSAC and SSACFFT during high-temperature curing were measured using 3D laser scanning. The results showed that the SSAs in concrete expand and cause cracking/spalling during hydration, which is effectively restrained by the FRP tube. The strength, failure modes and stress–strain relationships of the SSACFFT were investigated via axial compression tests. Finally, the SSACFFT was proposed as a prefabricated structural component called FRP-tube-confined concrete core encased prestressed rebar (FCCC-PR) to capitalize on the volume expansion characteristic of SSAC.

### 1. Introduction

Steel slag is a byproduct of steel production composed of CaO, SiO<sub>2</sub>, Al<sub>2</sub>O<sub>3</sub>, FeO, MgO, MnO and P<sub>2</sub>O<sub>5</sub> and makes up approximately 15% of steel output [1]. China's crude steel output was 1053.0 million tons in 2020 according to the China Statistical Yearbook [2], and steel slag production exceeded 150 million tons. Annually produced in a large quantity, steel slag leads to the occupation of farmland and serious pollution of the environment [3,4]. The reasonable utilization of steel slag is important for resolving these problems. Characterized as having hard, wear-resistant, adhesive and rough features, steel slag has been a very useful aggregate in concrete [5]. Fan et al., [6] added steel slag powder to ultra high-performance concrete (UHPC) and analyzed the influence of addition on the mechanical performance. Liu et al., [7] proposed a high-performance carbonatable concrete adopting steel slag powder as binders, whose performance was comparable to that of UHPC. Research on steel slag aggregates (SSAs) has attracted the attention of many researchers since the 2000 s. The behaviors of SSAs in concrete serving as coarse aggregates [8–11], fine aggregates [8,12,13], or both

coarse and fine aggregates [14] and raw materials for lightweight aggregates [15] have been investigated, proving that the introduction of steel slag can create good economic and environmental effects. Liu et al., [16,17] also added steel slag as coarse aggregates to UHPC and analyzed the contents, structure and mechanical performance of this eco-friendly UHPC. The utilization of steel slag as aggregates is not limited to cement-based materials. Sun et al., [18] replaced natural limestone aggregates with basic oxygen furnace (BOF) steel slag aggregate in metakaolin-based geopolymers and found that the replacement could improve workability and strength. In recent years, an increasing number of researchers have focused on the environmental effect on the performance of SSAC. Papachristoforou et al., [19] investigated the performance of steel fiber-reinforced concrete with coarse SSA under dry, freeze–thaw and elevated temperature conditions. Andrade et al., [20] investigated the mechanical performance and resistance to carbonation of SSAC, and the results corroborated its technical feasibility. Malathy et al., [21] treated the surface of energy optimized furnace (EOF) steel slag with fly ash to improve the corrosion resistance of steel slag, which also promoted the use of SSAC.

\* Corresponding author at: Department of Civil Engineering, Tsinghua University, Beijing 100084, China.

E-mail addresses: [fengpeng@tsinghua.edu.cn](mailto:fengpeng@tsinghua.edu.cn) (P. Feng), [lizhiyua18@mails.tsinghua.edu.cn](mailto:lizhiyua18@mails.tsinghua.edu.cn) (Z. Li), [yangjiaqi@cumb.edu.cn](mailto:yangjiaqi@cumb.edu.cn) (J.-Q. Yang).

<https://doi.org/10.1016/j.conbuildmat.2021.125961>

Received 28 July 2020; Received in revised form 4 November 2021; Accepted 28 November 2021

Available online 28 December 2021

0950-0618/© 2021 Elsevier Ltd. All rights reserved.

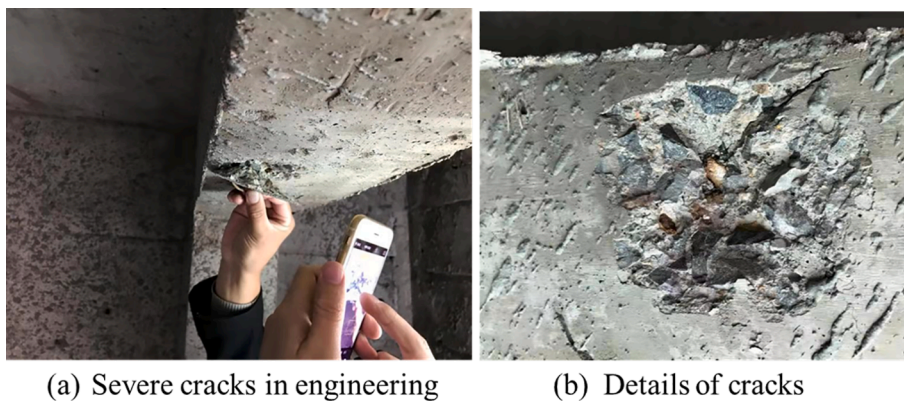


Fig. 1. Severe cracks caused by the SSAC (Courtesy of Dr. Tingyu Hao).



Fig. 2. Specimens.

However, steel slag aggregate concrete (SSAC) is not commonly utilized in many applications, especially as a structural material. This result arises because buildings and roads show severe burst cracks when adopting SSAC, causing serious quality problems and substantial economic losses (as shown in Fig. 1). SSAC can only be adopted in nonstructural members, for example, in gamma radiation shielding [22,23] or as weights to increase the resistance to the buoyancy of basements. This outcome is because of the potential of SSAC to contain high contents of free calcium and magnesium oxides, which expand when hydrated [24–27]. This phenomenon produces internal pressure and causes surface protrusion and cracks [26]. Hence, Kuo and Shu [28] suggested that careful consideration is required when replacing natural

aggregates with electric arc furnace oxidizing slags. Steel slag disposal in the construction industry requires improvement, and more effective methods are still being explored.

Fiber-reinforced polymer (FRP) is a kind of composite material made of fiber and matrix with a high strength-mass ratio and good corrosion resistance and is widely used in civil engineering, especially offshore engineering [29,30] and industrial engineering [31]. A concrete filled-in FRP tube (CFFT) is an effective application of FRPs in civil engineering, which could exploit the high tensile strength of the FRP material and compressive strength increase under confinement [32]. Different kinds of cementitious materials, such as coral aggregate concrete [33], engineered cementitious composites [34], and 3D printed gypsum [35], can be confined by FRPs, increasing the strength by 2–5 times. A general methodology used to build models for FRP-confined concrete [36,37] was presented. CFFT can be combined with steel rebars [38], steel tubes [31,35,39,40], cross-shaped steel [41,42] and other components [43] that are characterized by high strength, large deformability, bilinear behavior and good durability to satisfy both the serviceability and ultimate limit states. FRP tubes can be used as the framework and for the external confinement of concrete to increase its strength and ductility.

Table 2  
Mix proportions.

Series	Cement	Water	Sand	Limestone	Steel slag
P0	450	210	435	1305	0
P50	450	210	435	652.5	652.5
P100	450	210	435	0	1305

Table 1  
List of specimens.

Series	Specimen	Type of confinement	Percentage of steel slag in the coarse aggregate
N-P0	N-P0-I	Non-confined	0%
	N-P0-II		
	N-P0-III		
N-P50	N-P0-I	Non-confined	50%
	N-P0-II		
	N-P0-III		
C-P50	C-P50-I	FRP cloth wrapped	50%
	C-P50-II		
	C-P50-III		
T-P0	T-P0-I	FRP tube encased	0
	T-P0-II		
	T-P0-III		
T-P50	T-P50-I	FRP tube encased	50%
	T-P50-II		
	T-P50-III		
T-P100	T-P100-I	FRP tube encased	100%
	T-P100-II		
	T-P100-III		

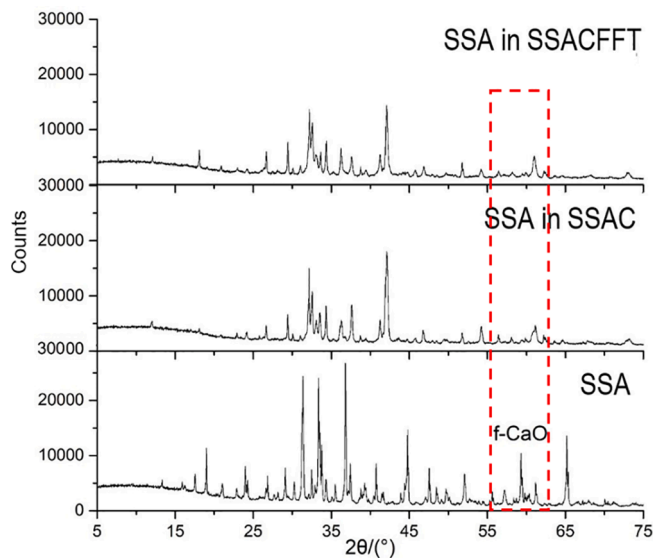


Fig. 3. XRD analysis of the SSAs.

Table 3  
Material properties of the FRP tube.

Material characteristics	Unit	Manufacturer data	Experimental data
Thickness	mm	/	3.06
Fiber volume	%	/	76.0
Glass transition temperature	°C	≥115	120
Hoop tensile stiffness	GPa	/	45.4
Hoop tensile strength	MPa	greater than 700	805

Table 4  
Material properties of the glass fiber sheet.

Nominal thickness (mm)	Fabric width (mm)	Elastic modulus (GPa)	Tensile strength (MPa)	Ultimate tensile strain (%)
0.169	500	100	2413	2.5

However, the shrinkage of filled concrete can cause an interface gap effect and postpone the confining effect, resulting in a decrease in the strength in the specified deformation [44]. Substituting the internal concrete of the CFFT by SSAC can largely solve this problem. Meanwhile, the FRP tube confines the SSAC and prevents excessive expansion, which in turn activates the confining effect on the internal SSAC.

Feng et al., [35,39] proposed the concept of an FRP-tube confined concrete core (FCCC). FCCCs share the same mechanism with CFFTs. Considering that CFFTs have poor performance under eccentric loading and that it is not economical or safe to use CFFTs as independent

structural members, the concept of the FRP-tube confined concrete core (FCCC) was proposed, which means that the FCCC is adopted as the structural component and is assumed to be a reinforcement with a high compressive strength. By a reasonable arrangement, the FCCCs can sustain the majority of the compression force applied to the cross section of the column, hence fully exploiting the compressive capacity of the confined concrete. Considering load uncertainty in practical applications, the tensile performance of FCCCs is vital. To overcome this drawback of FCCCs, Wang et al., [38] proposed the concept of FCCC-encased rebar (FCCC-R) by inserting a longitudinal steel bar into an FCCC. Furthermore, Feng et al., [45] improved FCCC-R by introducing prestress into the FCCC-R component, creating FCCC-encased prestressed rebar (FCCC-PR). Filling SSAC in FCCC-PR could be another effective application of SSAC. FCCC-PR could be produced and steam cured as prefabricated components in manufacturing, which could cause SSAC to expand to increase the prestress level and decrease the negative influence of SSAC during the usage stage.

Using an FRP as the confining material of SSAC is a possible solution to uncontrollable expansion, which leads to surface spalling and premature cracking of SSAC. In this paper, a steel slag aggregate concrete filled-in FRP tube (SSACFFT) is proposed. Facing the quality problem of SSAC, existing research has generally concentrated on the expansion mechanism of SSA and the method used to reduce it or the suggested percentage of SSA in aggregates. An effective and easy application that could accept the expansion of SSA and poor quality of SSAC was proposed in this paper, which is a groundbreaking idea. In particular, there are no additional processing and usage limits for SSAs, which would be more attractive for construction units. However, there has been a lack of studies regarding the quantification of the volume expansion of SSAC and the mechanical properties of FRP-confined SSAC under axial compression. To fill these knowledge gaps, experimental investigations were carried out and are reported in this paper.

The volume expansion effect of the SSACFFT was investigated by the 3D laser scanning method during concrete high-temperature curing. The results showed that the steel slag used as coarse aggregates in concrete expands and causes premature cracks during the hydration reaction process, which can be distinctly limited by the FRP tube. Axial compressive tests were carried out on the SSACFFT. The strength, failure modes and stress-strain relations of the SSACFFT were determined based on the experiment. Based on the experimental results, the strength and the stress-strain relations of the SSACFFT were compared with the design-oriented FRP-confined concrete model, which indicates that the SSACFFT could be designed based on the existing model. Finally, adopting SSACFFTs as structural components, which are called FCCC-PR components, and forming prefabricated components in manufacturing were proposed in this paper, which seems to be a practical application approach.

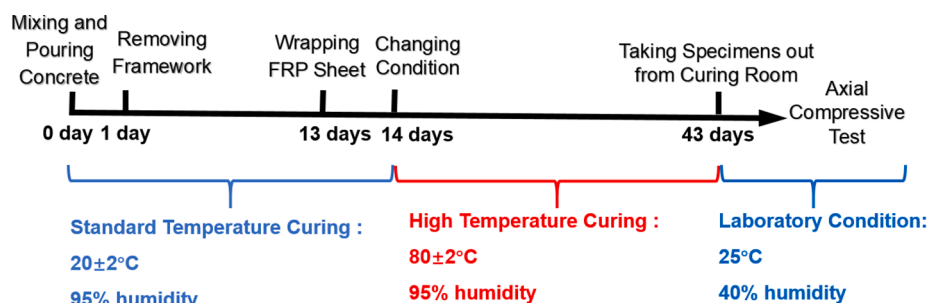


Fig. 4. Experimental process.

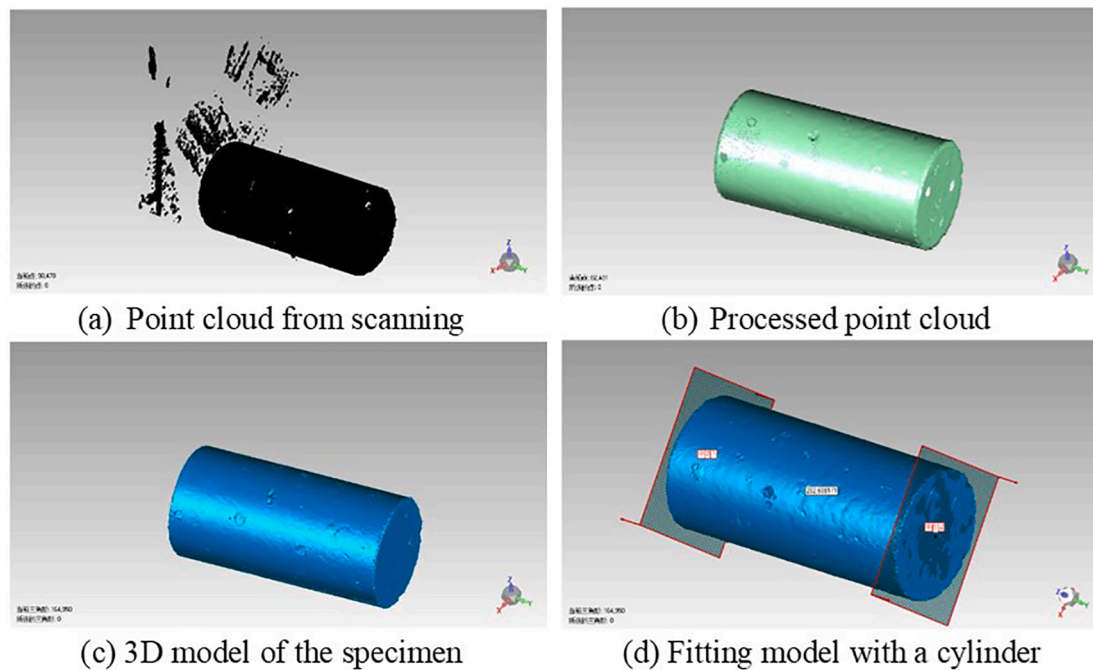


Fig. 5. Specimens scanned by 3D laser scanning.

## 2. Experimental study

### 2.1. Test specimens

A total of 18 cylindrical specimens were prepared and tested, comprising 6 groups of specimens (Fig. 2). All specimens had a diameter of 100 mm (diameter of the concrete core) and a height of 200 mm. The percentage of steel slag coarse aggregates (0%, 50% and 100%) and the type of confinement (nonconfined, FRP sheet-wrapped and FRP tube-encased) were taken as the experimental parameters. Three identical specimens were repeatedly evaluated for each permutation of the test parameters. The test specimens were labeled by the following rules: [Confinement]-[Percentage of SSAs] [Repeated number of tests] (N for unconfined, C for wrapped FRP sheets, and T for an encased FRP tube). For example, T-P50-II is the second FRP tube-encased specimen with 50% SSA replacement. Details of all the specimens are summarized in Table 1.

### 2.2. Material properties

#### 2.2.1. Concrete

The target strength grade of the concrete used in the trials was C40, and steel slag (converter steel slag) was adopted as coarse aggregate to replace part of the crushed limestone, with replacement percentages of 0%, 50% and 100%. The maximum particle size of the coarse aggregate was 20 mm. The specific mix proportions were designed according to the “Specification for Mix Proportion Design of Ordinary Concrete JGJ55-2011” [46]. The binder material used in this study was Portland cement (P.O. 42.5 as per Chinese Standard GB175). The sand percentage was 33%, and the W/B ratio was 0.47. No fly ash or water reducing agent was added to the mixture. The mix proportions of each series are listed in Table 2. The concrete paste volume was 27.5%. A lower paste volume could increase the strength and quality of concrete [47].

#### 2.2.2. XRD analysis of the SSA

Before the volume measurement and the axial compressive test, X-ray diffraction (XRD) was carried out to investigate whether the FRP influenced hydration of the SSA. Wang et al., [25] investigated the compressive strength of SSAC over a time span of 4 years and found that

free calcium oxide f-CaO is the primary component that leads to the expansion of the SSA. Therefore, detection of f-CaO is an essential part of XRD analysis. Fig. 3 shows the XRD patterns of SSAs, SSAs in SSAC and SSAs in the SSACFFT. According to the XRD analysis, the SSAs contain f-CaO, whereas no f-CaO could be observed in the SSAs in SSAC or SSAs in the SSACFFT, which illustrates the full reaction of f-CaO. In conclusion, the FRP tube had very little influence on the hydration of SSAs, and SSAs in the SSACFFT expanded like the SSAs in SSAC.

#### 2.2.3. FRP tube

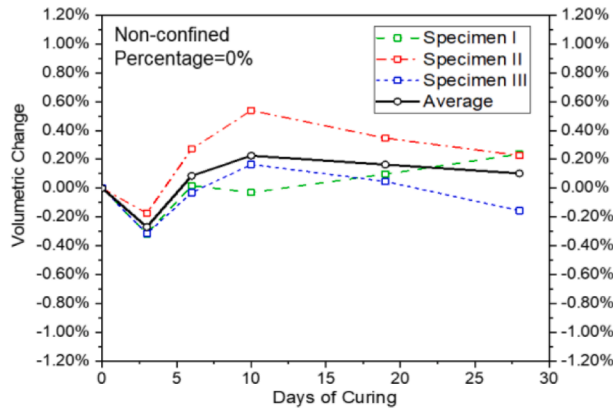
The FRP tubes used in this experiment were manufactured via the filament winding process using E-glass fibers and anhydride cured epoxy resin produced by Sinoma Jinjing Glass Fiber Co., Ltd. The FRP tubes were designed with a fiber volume fraction of 70% and fiber angles of  $\pm 85^\circ$  (the angle between the fiber and the longitudinal axis of the tube). The detailed material properties are shown in Table 3.

#### 2.2.4. FRP sheet-wrapped specimens

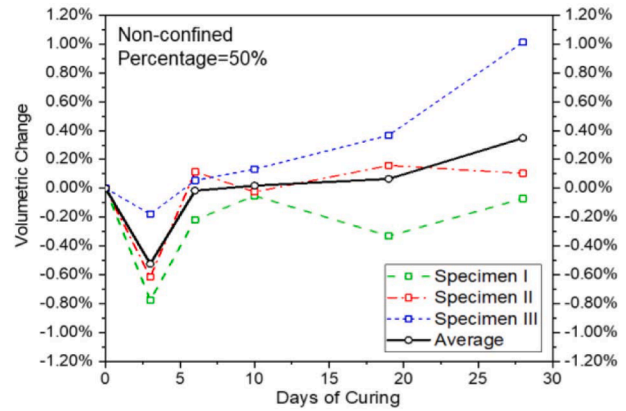
For the FRP sheet-wrapped specimens, a six-ply glass fabric with a total nominal thickness of 1.014 mm was used for wrapping. The material properties of the glass fabric are listed in Table 4, which was provided by the manufacturer.

The concrete cylinders were cast in a mold made of polyvinyl chloride (PVC) tubes until solidifying (one day after casting). After removing the mold, the concrete was cured under standard curing conditions (“Standard for the Test Method of Mechanical Properties of Ordinary Concrete GB/T 50081-2002” [48], with a temperature of  $20 \pm 2^\circ\text{C}$  and humidity above 95%) for 14 days. After curing, the cylinders were wrapped with continuous fiber sheets in the hoop direction, with a total length of 2000 mm, resulting in 6 layers of wrapping and an overlap length of approximately 115 mm. In addition, at both ends of the cylinder, two extra strips with widths of 25 mm and total lengths of 2000 mm were applied to prevent end crushing of the specimens. During the wrapping process, a two-part building structural adhesive was applied and saturated into the fiber fabric.

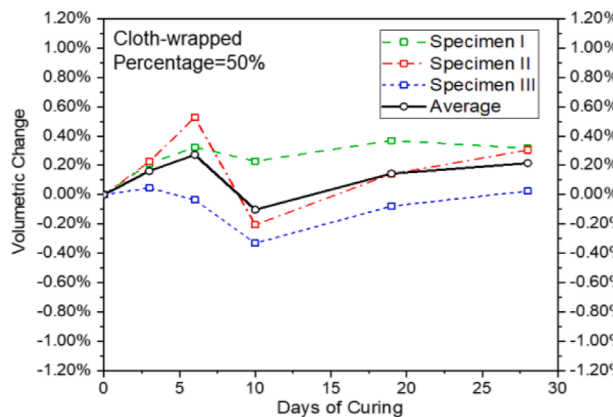
After the wrapping process and the adhesive solidified, the specimens were cured under high-temperature curing conditions (the temperature was  $80 \pm 2^\circ\text{C}$ , and the humidity was above 95%) before the tests were carried out.



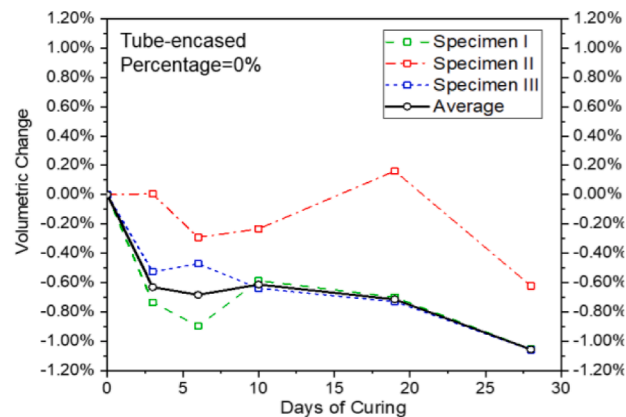
(a) N-P0 Series



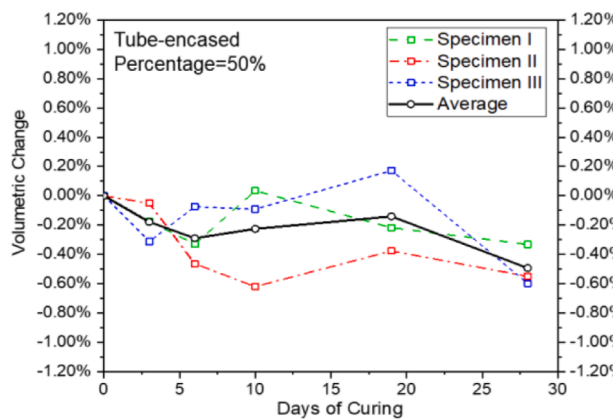
(b) N-P50 Series



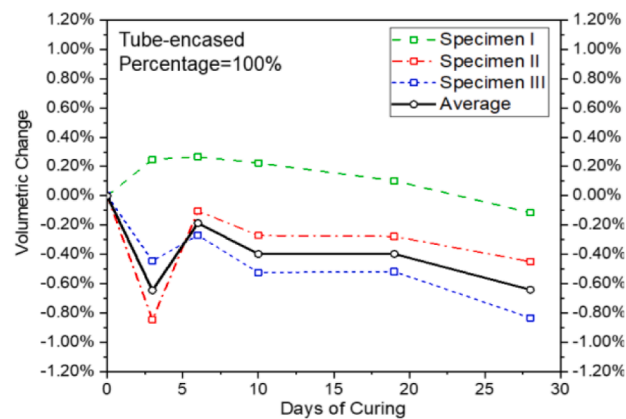
(c) C-P50 Series



(d) T-P0 Series



(e) T-P50 Series



(f) T-P100 Series

Fig. 6. Volumetric change percentage curves.

### 3. Volume expansion effect

SSAs can have a high content of free calcium and magnesium oxides, which expand when hydrated and lead to an increase in the SSAC volume [24,25]. To evaluate volumetric changes in the SSAC and SSACFFT, 3D laser scanning was adopted to measure the specimen volumes.

3D laser scanning is an emerging technology that can capture the geometric characteristics of a measured object with laser equipment that

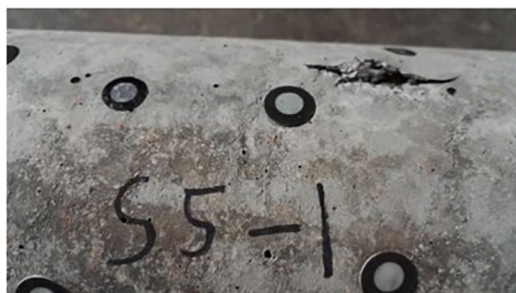
measures the distance between the scanner and the object. This method has been widely used in the quality evaluation and monitoring of structural engineering and geotechnical engineering [49–51]. Kim et al., [52,53] combined 3D laser scanning with building information modeling (BIM) to develop a systematic and practical approach for the dimensional and surface quality assessment of precast concrete elements; this technique proves the feasibility of obtaining the geometrical data of concrete by 3D laser scanning.

**Table 5**  
Volumetric change in the specimen during curing.

Series	Specimen	Initial volume/mm <sup>3</sup>	$\Delta V_3$	$\overline{\Delta V}_3$	$\Delta V_6$	$\overline{\Delta V}_6$	$\Delta V_{10}$	$\overline{\Delta V}_{10}$	$\Delta V_{19}$	$\overline{\Delta V}_{19}$	$\Delta V_{28}$	$\overline{\Delta V}_{28}$
N-P0	N-P0-I	1,781,303	-0.32%	-0.27%	0.02%	0.09%	-0.03%	0.23%	0.10%	0.16%	0.24%	0.10%
	N-P0-II	1,789,439	-0.17%		0.27%		0.54%		0.35%		0.23%	
	N-P0-III	1,797,347	-0.32%		-0.03%		0.17%		0.05%		-0.16%	
N-P50	N-P0-I	1,799,891	-0.78%	-0.52%	-0.22%	-0.02%	-0.05%	0.02%	-0.33%	0.07%	-0.07%	0.35%
	N-P0-II	1,808,381	-0.62%		0.11%		-0.03%		0.16%		0.10%	
	N-P0-III	1,818,320	-0.18%		0.05%		0.13%		0.37%		1.01%	
C-P50	C-P50-I	1,858,294	0.21%	0.16%	0.32%	0.27%	0.23%	-0.10%	0.37%	0.14%	0.32%	0.22%
	C-P50-II	1,869,348	0.23%		0.53%		-0.21%		0.14%		0.31%	
	C-P50-III	1,893,064	0.05%		-0.04%		-0.33%		-0.08%		0.03%	
T-P0	T-P0-I	1,791,000	-0.73%	-0.63%	-0.90%	-0.68%	-0.59%	-0.61%	-0.70%	-0.71%	-1.05%	-1.06%
	T-P0-II*	1,787,884	0.01%		-0.29%		-0.23%		0.16%		-0.62%	
	T-P0-III	1,800,274	-0.53%		-0.47%		-0.64%		-0.73%		-1.06%	
T-P50	T-P50-I	1,635,187	-0.17%	-0.18%	-0.33%	-0.29%	0.04%	-0.23%	-0.22%	-0.14%	-0.33%	-0.49%
	T-P50-II	1,554,571	-0.05%		-0.46%		-0.62%		-0.38%		-0.55%	
	T-P50-III	1,591,807	-0.31%		-0.07%		-0.09%		0.17%		-0.60%	
T-P100	T-P100-I*	1,574,850	0.25%	-0.65%	0.27%	-0.19%	0.22%	-0.40%	0.10%	-0.40%	-0.12%	-0.64%
	T-P100-II	1,590,310	-0.85%		-0.10%		-0.27%		-0.28%		-0.45%	
	T-P100-III	1,574,629	-0.44%		-0.27%		-0.52%		-0.52%		-0.83%	

$\Delta V_t$  stands for the volumetric change after t days of curing, and  $\overline{\Delta V}_t$  stands for the average volumetric change after t days of curing.

\* T-P0-II and T-P100-I are not considered in the calculation of the average and standard deviation because of too much deviation compared with other specimens from the same series.



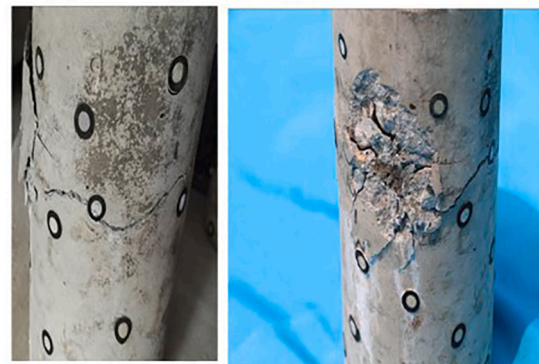
(a) Six days' curing of N-P50-I



(b) Ten days' curing of N-P50-I



(c) Nineteen days' curing of N-P50-III



(d) Twenty eight days' curing of N-P50-III

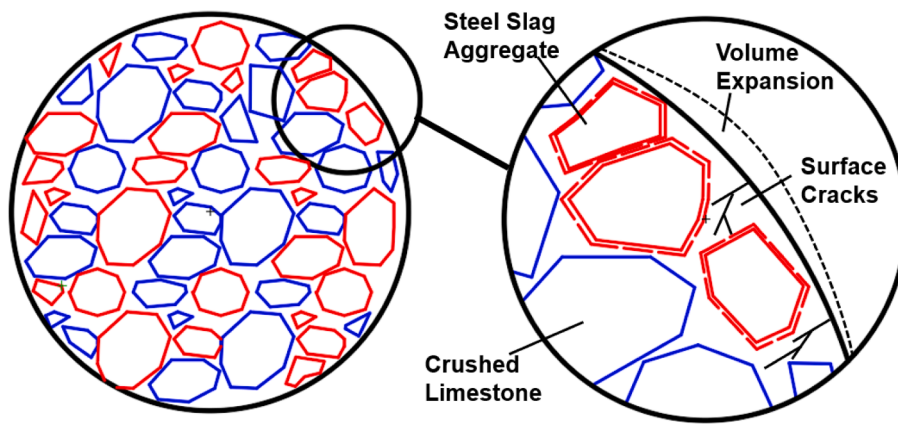
**Fig. 7.** Spalling of the SSAC.

Because the reaction rate of the SSA is relatively low, high-temperature conditions are used to cure the concrete specimens to accelerate expansion so that the long-term performance of SSAC specimens can be simulated. After removing the molds and 14 days of standard curing (the temperature was  $20 \pm 2$  °C, and the humidity was above 95%), all specimens were moved to a high-temperature curing chamber (the temperature was  $80 \pm 2$  °C, and the humidity was above 95%) for 28 days. During high-temperature curing, the volume of the specimens was measured six times. The entire experimental process is shown in Fig. 4.

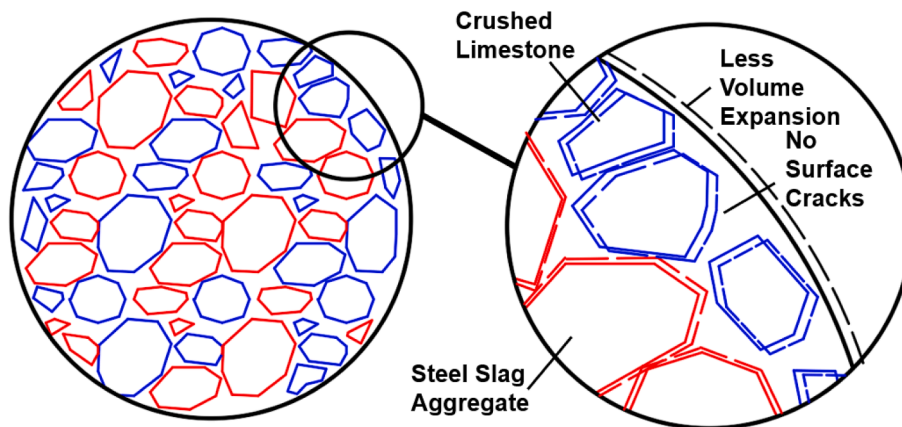
### 3.1. 3D laser scanning

3D scanning technology is an emerging measurement technology that uses laser scanning to obtain the point cloud of an object surface combined with computer technology to calculate the geometric data and model. This technique has the advantages of noncontact measurement, a high accuracy and a high efficiency and has been used to measure the initial defects of steel and evaluate the quality of concrete in the existing literature [49,50,52,53].

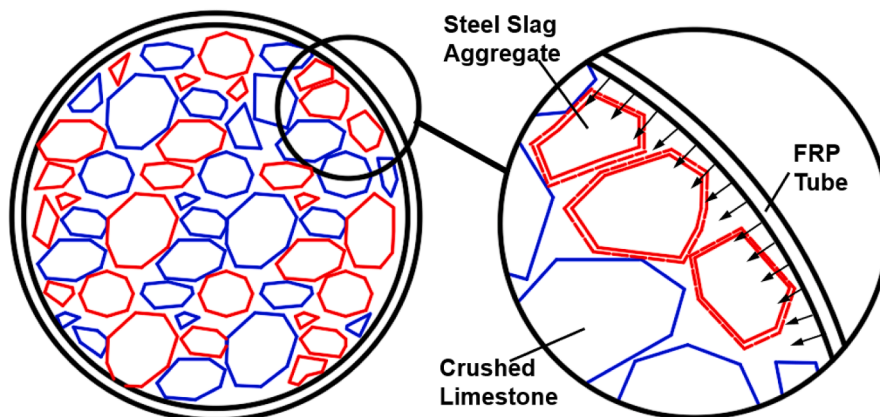
A handheld scanner produced by Beijing Tianyuan Three-Dimensional Technology Co., Ltd., which consisted of laser



(a) Cross section of the SSAC with surface cracks



(b) Cross section of the SSAC with no surface cracks



(c) Cross section of the SSACFFT

Fig. 8. Cross-sections of the specimens.

transmitters and charge-coupled device (CCD) cameras with high resolution and high frequency, was adopted in this study. The handheld 3D laser scanner has a 0.02 mm positioning accuracy, which fulfills the requirements of the volume measurement in this study. To coordinate the scanned object, spatial reflective marker points were evenly sprayed onto the surface and the surrounding environment and could be identified by CCD cameras. After that, a laser array was projected on the surface of the object to create a light profile. Photographic recording of the light profile was performed by CCD cameras to locate the points on

the light profile and form the point cloud (as shown in Fig. 5a), whose coordinates were calculated according to the relative distance between the scanned points and the marker points (at least three marker points are needed). During scanning, the handheld scanner and the scanned object can be moved freely to scan from different angles. Hence, the overall shape of the measured object can be determined with improved accuracy.

The point cloud from scanning should be processed carefully by deleting noise points apart from the specimen (as shown in Fig. 5b) to

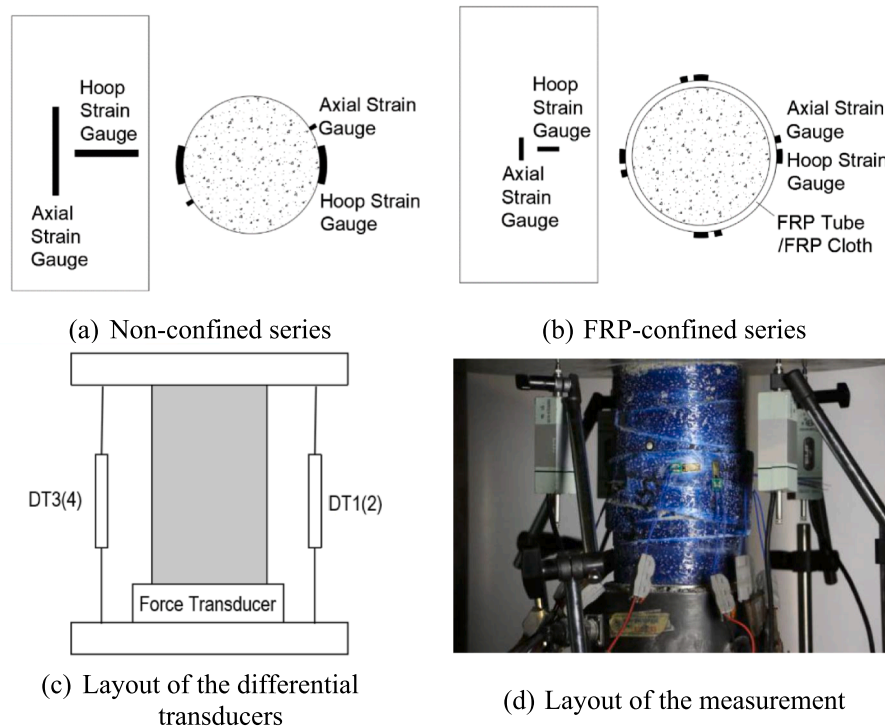


Fig. 9. Layout of the measurement.

prevent the noise points' influence on the modeling accuracy. Based on the processed discrete point cloud, a 3D model of the specimen was built by Geomagic Studio 2014 from Geomagic (as shown in Fig. 5c). For the unconfined SSAC specimens, nonuniform expansion can be captured by the software. Because of the covering of the FRP tube/cloth, lateral expansion of the FRP-confined SSAC cylinders was restrained by the FRP tube or the wrapped FRP sheet, the volumetric change was mainly in the axial direction, and the volumetric change of that lateral surface was insignificant. Using the cylindrical fitting function of Geomagic Studio 2014, the changes in the cylinders' heights were measured (as shown in Fig. 5d).

### 3.2. Test results

The volume of the specimens was measured, and the phenomena of the specimens were measured before and after 3, 6, 10, 19 and 28 days of curing and after 6 days of high-temperature curing. The volumetric change curves are shown in Fig. 6, and detailed data are reported in Table 5.

#### 3.2.1. Unconfined SSAC

After 3 days of curing, no obvious change was observed on the surface of the N-P50 series specimens.

After 6 days of curing, surface cracks caused by aggregate expansion were observed in N-P50-I as shown in Fig. 7a. Through the largest crack, a dark internal surface of the cracked area and shattered SSAs were observed, having the same phenomena as SSAC in engineering applications, as shown in Fig. 1.

After 10 days of curing, the cover of the cracked area peeled off from the specimen as shown in Fig. 7b. In addition, more tiny cracks were observed on the top surface of N-P50-I and the lateral surface of N-P50-III.

After 19 days of curing, cracks developed gradually on N-P50-III as shown in Fig. 7c. However, cracks did not develop on N-P50-I because the internal expansion pressure released when the concrete cover peeled.

After 28 days of curing, N-P50-III had serious cracking damage, as

shown in Fig. 7d. Expansion of the SSA caused wide transverse cracks to form on the surface of the specimen, which almost propagated through the entire cross section of the specimen and had a maximum width of 3 mm. Similar to that of N-P50-I, the cover of the cracked area peeled off, and shattered SSA was seen in N-P50-III.

The volumetric change percentage curve of SSAC during 28 days of curing could be drawn based on the volume calculated by Geomagic Studio 2014 (as shown in Fig. 7b). To demonstrate the influence of the SSA more clearly, the volumetric change percentage curve of ordinary aggregate concrete (OAC) (N-P0 series) during 28 days of curing was also plotted as a control group (as shown in Fig. 6a). During the early stage (0–3 days), the volume of OAC specimens decreased because of shrinkage, followed by a distinct increase in the middle stage (3–6 days). Next, the increase slowed down during the last stage (6–28 days). The decrease in N-P50-I during 10–19 days of curing corresponded to the peeling of the concrete cover, and the sudden increase in N-P50-III during 19–28 days of curing corresponded to the distinct expansion in the axial direction caused by the wide transverse crack.

The volume expansion effect was distinct except for that of N-P50-II. The variations between specimens could probably be explained by the SSA distribution. If there are more SSAs located near the surface of a specimen, then there will be severe surface cracks (e.g., N-P50-I and N-P50-III, as shown in Fig. 8a) because of the weak confinement effect of the cover. In contrast, if more crushed limestone aggregates are located near the surface, then the outer layer of the specimen can provide stronger confinement effects to limit the expansion of the internal SSAs (e.g., N-P50-II, as shown in Fig. 8b), which results in fewer cracks and less volume expansion. Due to the randomness of the aggregate distribution and the lack of external confinement, the results of the N-P50 specimens demonstrate a significant variation, as shown in Fig. 6b.

#### 3.2.2. Volume expansion effect of the SSACFFT

There are no surface cracks found in the T-50 series and T-100 series of specimens because of the confinement of the FRP tube. In addition, shrinkage and height decrease were observed. The volumetric change percentage curves of the SSACFFT during the 28 days of curing are plotted in Fig. 6e and f, and the T-P0 specimens serve as the control

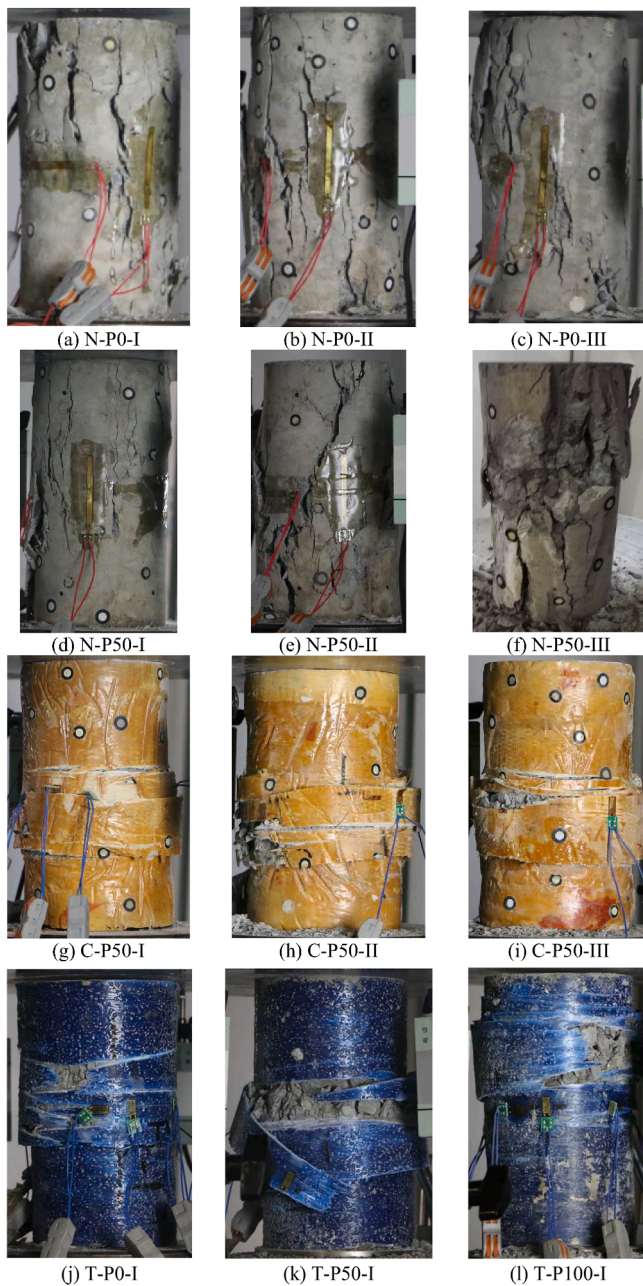


Fig. 10. Failure modes of the specimens.

group (as shown in Fig. 6d). Notably, T-P100-I and T-P0-II were excluded for calculating the average values because their values deviated too much compared to those of the specimens from the same series.

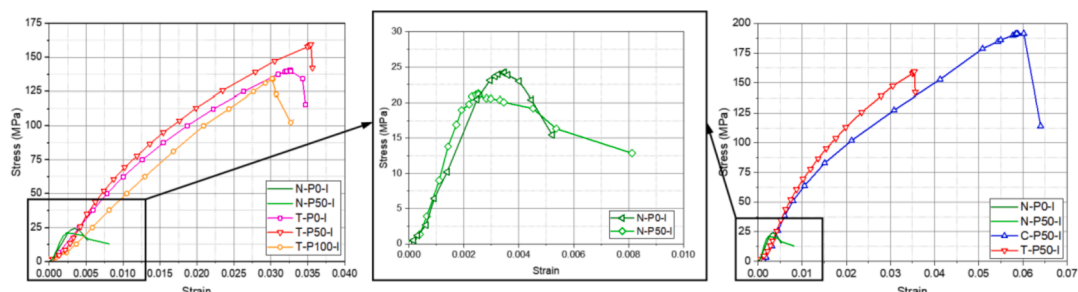


Fig. 11. Stress-strain curves of the specimens.

The SSACFFT specimens show the same trend as the SSAC during the early and middle stages despite varying amplitudes. Introduction of the FRP tube could decrease the extent of volume expansion during the 3–10 days of curing and could change volume expansion to shrinkage during the 19–28 days of curing according to the comparison between the T-P50 series and N-P50 series.

The mechanism of the SSACFFT is explained in Fig. 8c. Similar to SSAs in the N-P50 series, these SSAs expand during hydration. Despite the random distribution of SSAs, volumetric expansion was relatively limited because of the confinement of the external tube.

On the other hand, replacing OAC with SSAC in FRP tubes is also of great significance. Shrinkage of filled concrete can cause an interface gap effect and postpone the confining effect, resulting in a decrease in the strength in the specified deformation. According to the scanned results, the SSAC in the FRP tube shows less volume reduction than the OAC in the FRP tube.

The T-P50 series shows a larger variation than the T-P100 series, which supports the hypothesis proposed in section 3.2.1 and indicates that the variation in N-50 was caused by the randomness of the SSA distribution rather than the steel slag expansion effect.

In general, SSAC tends to expand compared with OAC. More specifically, for unconfined cylinders, the average volume change rate for SSAC (N-P50) of + 0.35% was higher than that for OAC (N-P0) of + 0.1% after 28 days of curing. Once the cylinders were confined by the FRP tube, both the OAC and SSAC shrank, and SSAC shrank less than OAC. Additionally, the content of steel slag did not have an obvious influence on the trend of the volume change. There are two possible reasons for the shrinkage of the SSACFFT. First, note that the first volume measurement was performed immediately after standard curing. Lateral expansion of the SSACFFT was restrained by the FRP tube at the standard curing stage, while the unconfined and FRP sheet-wrapped specimens were free to expand during this stage. Additionally, the cement tended to shrink after the hydration reaction. Therefore, once the surface crack of the SSAC was restrained at the early stage, expansion of the SSAs could be confined by the surrounding cement mortar, and the overall behavior of the specimen showed a decreasing volume. Second, the shrinkage can be attributed to the blocking effect of the FRP tube that blocked the entry of water and affected the degree of the hydration reaction. Nevertheless, the mechanisms for the interaction between the FRP and the hydration of the SSA still need to be investigated in the future. This study is beyond the scope of this work.

#### 4. Axial compressive experiments

##### 4.1. Loading conditions and measurements

The experiments were carried out under monotonic axial compression by a universal testing machine with a 2000 kN capacity. As shown in Fig. 9, the axial compression test specimens were measured by a force transducer, differential transducers and strain gauges. For the non-confined series, two axial strain gauges and two hoop strain gauges with a gauge length of 50 mm were installed on the lateral concrete surface,

**Table 6**  
Key test results of the specimens.

Series	Specimen	$f_{cc}$ (MPa)	$\epsilon_{cc}$ ( $\mu\epsilon$ )	$\epsilon_{h,rupt}$ ( $\mu\epsilon$ )	$f_{u,a}/f_{co}$	$f'_{cc}/f'_{co}$	$\epsilon_{cc}/\epsilon_{co}$
N-P0	N-P0-I	24.23	1719	–	–	–	–
	N-P0-II	24.58	1338	–	–	–	–
	N-P0-III	27.80	1315	–	–	–	–
	Average	25.54	1457	–	–	–	–
N-P50	N-P50-I	21.28	2535	–	–	–	–
	N-P50-II	30.43	3186	–	–	–	–
	N-P50-III	25.45	*	–	–	–	–
	Average	25.72	2861	–	–	–	–
C-P50	C-P50-I	191.51	28,979	**	–	7.50	19.89
	C-P50-II	185.31	32,435	19,158	1.51	7.26	22.26
	C-P50-III	175.10	33,811	19,648	1.54	6.86	23.21
	Average	183.97	31,742	19,403	1.53	7.20	21.79
T-P0	T-P0-I	143.69	27,023	11,351	1.22	5.63	18.55
	T-P0-II	159.08	29,033	13,643	1.47	6.23	19.93
	T-P0-III	151.82	26,279	12,414	1.34	5.94	18.04
	Average	151.53	27,445	12,469	1.34	5.93	18.84
T-P50	T-P50-I	162.75	22,200	14,120	1.52	6.37	15.24
	T-P50-II	142.36	25,566	9717	1.05	5.57	17.55
	T-P50-III***	120.35	14,476	7851	0.85	4.71	9.94
	Average	152.56	23,883	11,919	1.28	5.97	16.39
T-P100	T-P100-I	136.99	22,926	9243	1.00	5.36	15.74
	T-P100-II	146.64	23,077	11,073	1.19	5.74	15.84
	T-P100-III	152.78	25,913	11,337	1.22	5.98	17.79
	Average	145.47	23,972	10,551	1.14	5.70	16.45

\* The axial strains of N-P50-III were not measured because of severe cracks on the surface and no room for the strain gauges.

\*\* All hoop strain gauges failed before the FRP tube ruptured.

\*\*\* T-P50-III is not considered in the calculation of the average because of eccentric loading and too much deviation compared with other specimens from the same series.

which were bonded at the middle height of the specimen and evenly distributed along the circumference (as shown in Fig. 9a). On the other hand, for the FRP-confined series, four axial strain gauges and hoop strain gauges with a gauge length of 10 mm were installed on the lateral FRP surface at the middle height of the specimen and evenly distributed along the circumference (as shown in Fig. 9b). Four differential transducers measured the axial deformation of the overall specimen, which was evenly distributed on all four sides (as shown in Fig. 9c).

Prior to testing, all specimens were troweled by a mortar to ensure a uniform distribution of the applied load. Finally, load was applied on the full cross section of the specimens in a manually loaded controlled manner with a loading speed of 0.5 mm/min.

#### 4.2. Failure modes

For the N-P0 series (nonconfined OAC specimens), the failure modes of specimens I and II were mainly caused by parallel vertical cracks, while the upper part of specimen III cracked first, in which the crack extended diagonally to the lower part of the specimen and finally formed inclined splitting cracks, which were both common failure modes of nonconfined OAC specimens (as shown in Fig. 10a-c). The failure modes of specimens in the T-P0, T-P50 and T-P100 series were so similar that only representative specimens in these series were selected.

For N-P50-I and N-P50-III with poor casting quality after high-temperature curing, initial cracks developed severely during the experiment and caused the failure of the overall specimens (as shown in Fig. 10d-f). In contrast, N-P50-II showed the same failure mode as the OAC specimens with inclined splitting cracks (as shown in Fig. 10e).

For the FRP-confined series, 12 specimens showed similar behaviors: during the loading process, the sound of partial fiber breaking could be heard. At the ultimate load, fiber fractures rapidly extended to both sides along the angle of fibers (i.e.,  $\pm 85^\circ$  to the longitudinal axis of the tube) accompanied by the flowing out of internal crushed concrete, leading to the explosive failure of the specimen (as shown in Fig. 10(g)-(l)).

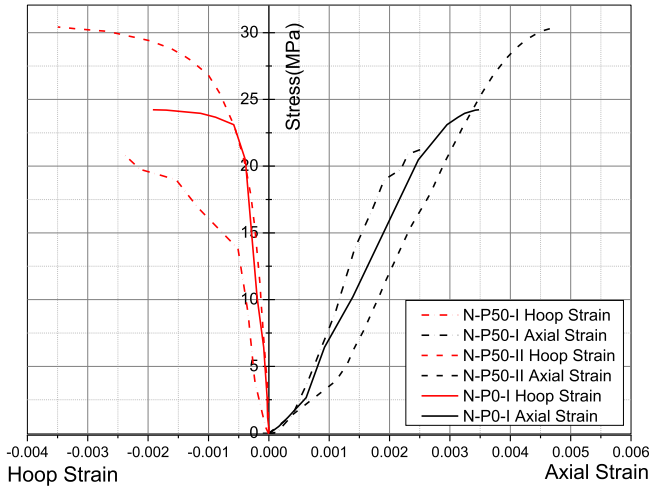
#### 4.3. Experimental results

The axial stress–strain curves of representative specimens from each series are shown in Fig. 11. When the concrete specimen approached the ultimate load, measured data from some strain gauges were missed due to the peeling of the concrete cover or the debonding of the strain gauges. Hence, axial strains were calculated based on measurements by differential transducers. The measured displacement represents the compressive deformation of the whole specimen, including the localized deformation at both ends due to the uneven end surfaces. Therefore, the initial stiffness of the stress–strain curves shown in Fig. 11 gradually increases at the beginning of loading. Key test results are reported in Table 6, including the peak axial stress ( $f'_{cc}$ ), the corresponding axial strain ( $\epsilon_{cc}$ ) and the hoop strain ( $\epsilon_{h,rupt}$ ) of the FRP tube at the ultimate load, where axial strains and hoop strains were averaged from strain gauges remaining available at the ultimate load. The strength and strain enhancement ratios (i.e.,  $f'_{cc}/f'_{co}$  and  $\epsilon_{cc}/\epsilon_{co}$ ) are also reported in Table 6. The N-P0 series and N-P50 series specimens have lower strength and ductility. The confined specimens show bilinear behavior, and the strength and strain enhancement ratios are more than 5.70 and 16.39, respectively.

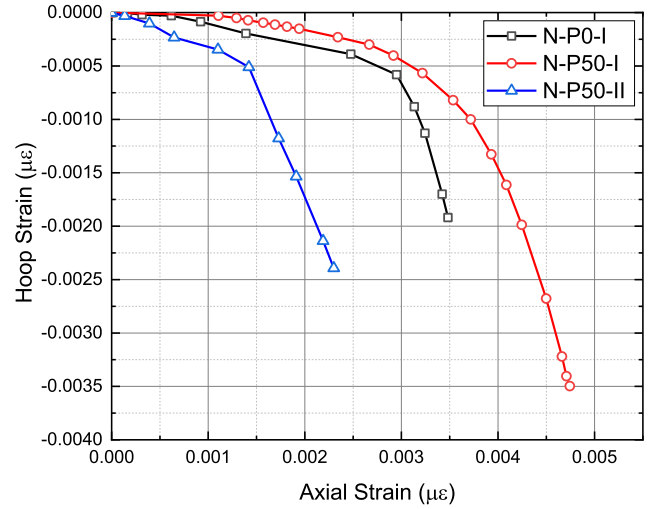
#### 4.4. Analysis of the results

To better analyze the influence of the SSAs and confinement, the axial stress–strain and axial stress-corresponding hoop strain curves and hoop strain-axial strain curves are shown in Figs. 12 and 13, respectively. In this paper, the compressive stresses/strains for concrete are defined as positive, whereas the tensile stresses/strains are defined as negative.

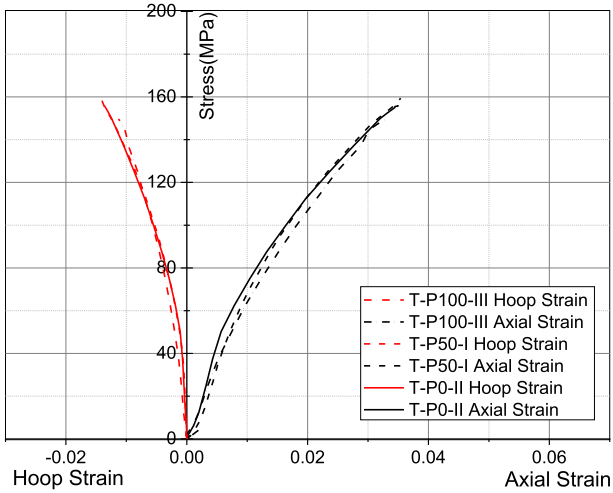
The axial compression results of three specimens, including one from the N-P0 series and two from the N-P50 series with (N-P50-I) or without (N-P50-II) spalling, are compared in Fig. 12a and 13a. According to Table 6, the average strengths of the two series are close (Ave. of N-P0 = 25.54 MPa and Ave. of N-P50 = 25.72 MPa), but the strength discreteness of SSAC is higher (standard deviation (S.D.) of N-P0 = 1.607 MPa and S.D. of N-P50 = 3.739 MPa). This result indicates



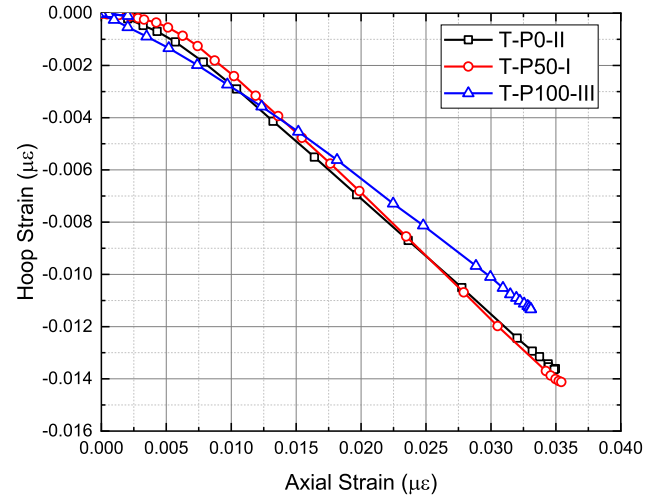
(a) Non-confined specimens with different percentages of the SSAC



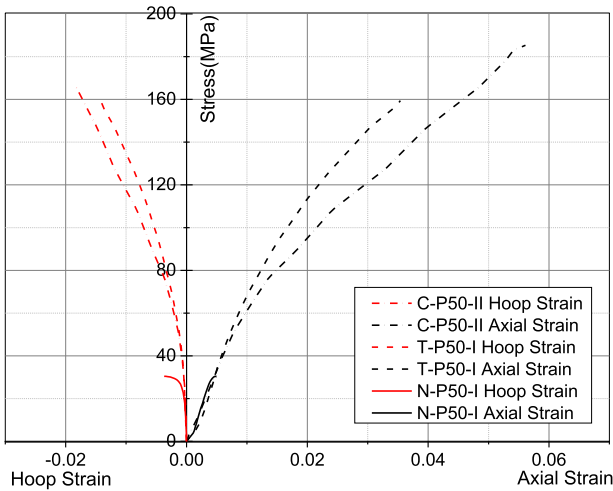
(a) Nonconfined specimens with different percentages of SSAC



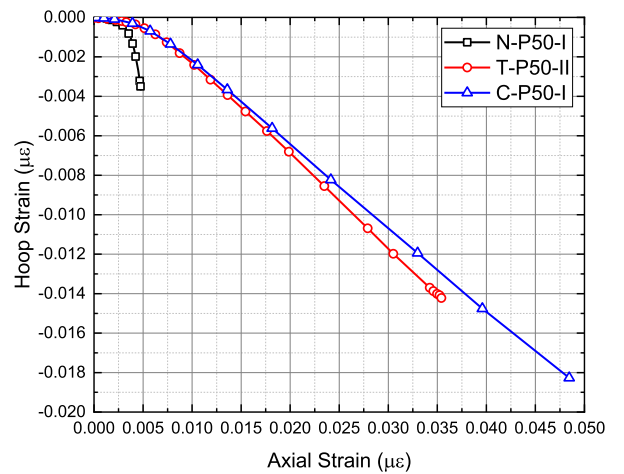
(b) CFFT specimens with different percentages of the SSAC



(b) CFFT specimens with different percentages of the SSAC



(c) Specimens under different confinements



(c) Specimens under different confinements

Fig. 12. Axial stress-axial and hoop strain curves.

Fig. 13. Hoop strain-axial strain curves.

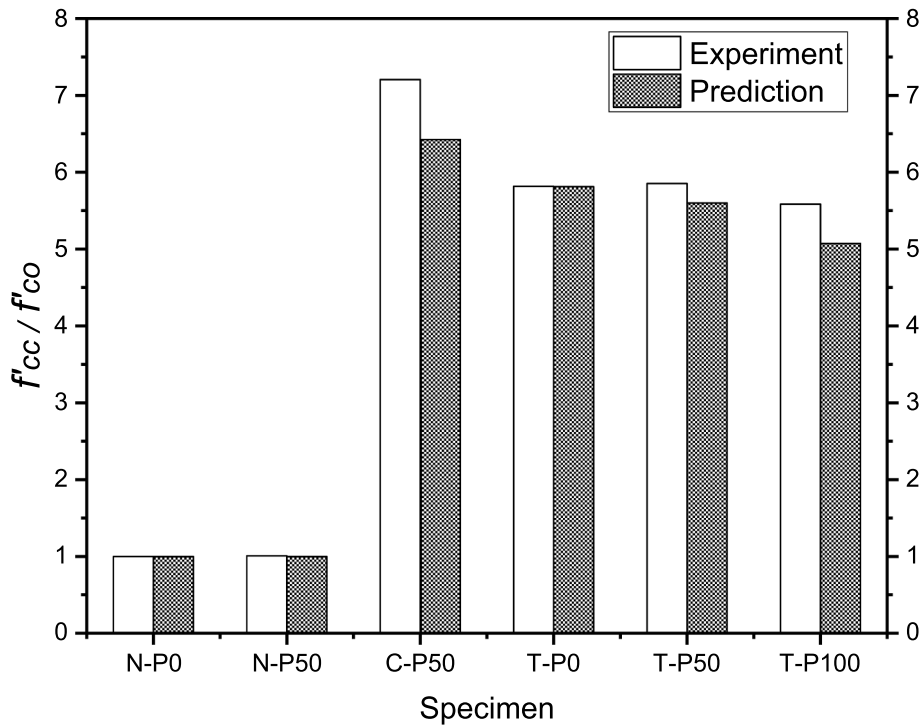


Fig. 14. Strength comparison of the experiment and prediction.

**Table 7**  
Strength comparison of the experiment and prediction.

Series	$\bar{\epsilon}_{h,rupt}$ ( $\mu\epsilon$ )	$f'_{cc,p}$ (MPa)	$\bar{f}'_{cc,t}$ (MPa)	Relative error*
C-P50	19,403	163.96	183.97	10.88%
T-P0	12,469	148.33	151.53	2.11%
T-P50	11,919	142.92	152.56	6.32%
T-P100	10,551	129.44	145.47	11.02%

$$*Relative\ error = \frac{f'_{cc,t} - f'_{cc,p}}{f'_{cc,p}} \times 100\%$$

that adding steel slag as the coarse aggregate has little influence on the strength of concrete. However, due to the expansion of the SSA, premature cracks developed in some specimens, resulting in a higher variation.

The axial compression results of representative specimens from the T-P0, T-P50 and T-P100 series, which were confined by FRP tubes with the same confinement ratio, are compared in Fig. 12b and 13b. Comparison shows that the mechanical behaviors of the three series of specimens are not very different. The hoop rupture strains in the SSACFFT are lower than those in the CFFT. As indicated by Dang et al., [34], the hoop rupture strain is influenced by the crack pattern of the

confined concrete. The test results suggest that fewer but wider major cracks formed in the internal concrete in the SSACFFT, leading to stress concentration in the FRP tube and resulting in a lower average value for the rupture hoop strain.

Hence, it can be concluded that under the confinement of the FRP tube, mixing steel slag as the coarse aggregate has no obvious influence on the axial compression performance.

#### 4.5. Comparison with the existing model

The design-oriented models for FRP-confined concrete proposed by Lam and Teng [54] have been widely used to predict or verify the strength and stress–strain curves for CFFTs. Based on the design-oriented model, Teng et al., [55] proposed refined design-oriented models. The strength in refined design-oriented models is shown in Equation (1):

$$\frac{f'_{cc}}{f'_{co}} = \begin{cases} 1 + 3.5(\rho_K - 0.01)\rho_\epsilon & \rho_K \geq 0.01 \\ 1 & \rho_K < 0.01 \end{cases} \quad (1)$$

where  $f'_{cc}$  = the ultimate axial stress of confined concrete and  $f'_{co}$  = the ultimate axial stress of unconfined concrete.

The parameter  $\rho_K$  is the confinement stiffness ratio, which is calcu-

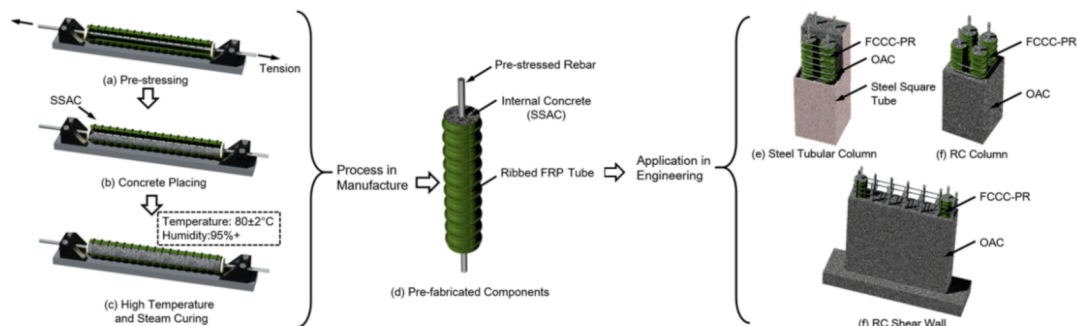


Fig. 15. Proposed application method of the SSAC.

lated by Equation (2):

$$\rho_K = \frac{2E_{FRP}t}{f'_{co}/\epsilon_{co}D} \quad (2)$$

where  $E_{FRP}$  = the elastic modulus of the FRP in the hoop direction;  $t$  = the thickness of the FRP sheet or the FRP tube;  $\epsilon_{co}$  = the ultimate axial strain of unconfined concrete; and  $D$  = the diameter of the confined concrete cylinder.

The parameter  $\rho_\epsilon$  is the strain ratio, which is calculated by Equation (3):

$$\rho_\epsilon = \frac{\epsilon_{h,rupt}}{\epsilon_{co}} \quad (3)$$

where  $\epsilon_{h,rupt}$  = the hoop rupture strain of the FRP sheet or the FRP tube.

The experimental results of SSAC are compared with the predictions from the refined design-oriented models for FRP-confined OAC in terms of the strength (as shown in Fig. 14 and Table 7). The strength of the CFFT shows good agreement with refined design-oriented models, and the strengths of the SSACFFT are higher than the predicted strength, which indicates that the SSACFFT designed by the refined design-oriented model is conservative.

## 5. SSAC filling-in FRP tube

In recent years, the authors' research group has developed a series of CFFT structural components, such as the FRP-tube confined concrete core (FCCC) [35,39], FCCC-encased rebar (FCCC-R) [38] and FCCC-encased prestressed rebar (FCCC-PR) [45], which has proven to be effective in improving the strength and ductility of reinforced concrete structural members. Filling SSAC in FCCC-PR could be an approach with reasonable mechanics and cost efficiency.

The application method is shown in Fig. 15. FCCC-PR can be produced in manufacturing by the pretensioning method, including the prestressed stage and concrete pouring stage. According to the axial compressive experiment, SSAC with a 100% SSA replacement rate can be placed in FCCC-PR, which would dispose of more steel slag. After the concrete-pouring stage, components need to be cured under high-temperature curing conditions (a temperature of  $80 \pm 2^\circ\text{C}$  and humidity above 95%) to cause the oxides to hydrate thoroughly, which decreases the SSC expansion extent during the service stage and increases the prestress level. Prefabricated components can be employed in steel tubular columns, RC columns, RC shear walls and other structural members whose external concrete is OAC with no volumetric expansion and good pouring quality.

## 6. Conclusions

Owing to the expansibility of SSAs, there is severe deterioration in the SSAC pouring quality and spalling in SSAC. Unlike the existing studies that have concentrated on improving the material performance, this paper concentrated on optimizing the application forms of SSAC and proposed the SSACFFT concept. Therefore, the following experiments were carried out. The long-term volume expansibility of SSAC and the long-term volumetric change in the SSACFFT were observed by 3D laser scanning technology under accelerated curing conditions. Axial compressive experiments were carried out on 18 specimens to investigate the mechanical behavior of the SSACFFT. Based on the results in this study, the following conclusions could be reached:

1) Without confinement, the SSAC expands after 28 days of high-temperature curing. Severe cracks may form and concrete cover spalling may occur on the surface of the specimens. The volume of the specimens increased by approximately 0.35%, on average.

- 2) The volume of the SSAC confined by the FRP tube decreased after 28 days of curing, and premature cracking or spalling of the SSAC was prevented.
- 3) The mechanical behavior of the SSACFFT is similar to that of an ordinary CFFT, and the existing design formulas are applicable to predict the strength of the SSACFFT.
- 4) The expansion of SSAC can reduce the interface gap and the postponing phenomenon of the confinement in the CFFT caused by the shrinkage of OAC. Thus, the stiffness of the SSACFFT is larger than that of the OACFFT.
- 5) The SSACFFT is an effective solution to overcome the poor quality, premature cracking and spalling of SSAC. This approach facilitates the massive recycling of SSAs as construction material for civil and infrastructure engineering. In particular, there are no additional processing and usage limits for SSAs, making them attractive for construction units.
- 6) Adopting SSAC in prestressed structural components can enhance the prestress level and reduce the prestress loss. This paper proposes that using SSAC in FCCC-PR is a possible future application of this material.

## CRediT authorship contribution statement

**Peng Feng:** Conceptualization, Validation, Project administration, Writing – review & editing, Supervision. **Zhiyuan Li:** Conceptualization, Investigation, Data curation, Formal analysis, Investigation, Visualization. **Shanbao Zhang:** Conceptualization, Investigation, Methodology. **Jia-Qi Yang:** Methodology, Data curation, Writing – review & editing.

## Declaration of Competing Interest

The authors declare that they have no known competing financial interests or personal relationships that could have appeared to influence the work reported in this paper.

## Acknowledgements

This work was supported by the National Natural Science Foundation of China (No. U2106219, 51978379, and 51908322), and the Institute of Guo Qiang, Tsinghua University (No. 2019QG1004 and 2021GQI0007).

## References

- [1] Q. Wang, P. Yan, J. Feng, A discussion on improving hydration activity of steel slag by altering its mineral compositions, *J. Hazard Mater.* 186 (2-3) (2011) 1070–1075, <https://doi.org/10.1016/j.jhazmat.2010.11.109>.
- [2] National Bureau of Statistics of China, *China statistical yearbook 2018*, China Statistics Press, Beijing, China, 2018.
- [3] J. Guo, Y. Bao, M. Wang, Steel slag in China: treatment, recycling, and management, *Waste Manag.* 78 (2018) 318–330, <https://doi.org/10.1016/j.wasman.2018.04.045>.
- [4] H. Yi, G. Xu, H. Cheng, J. Wang, Y. Wan, H. Chen, An overview of utilization of steel slag, *Procedia, Environ. Sci.* 16 (2012) 791–801, <https://doi.org/10.1016/j.proenv.2012.10.108>.
- [5] Y. Jiang, T.C. Ling, C. Shi, S.Y. Pan, Characteristics of steel slags and their use in cement and concrete—A review, *Resour. Conserv. Recycl.* 136 (2018) 187–197, <https://doi.org/10.1016/j.resconrec.2018.04.023>.
- [6] D. Fan, R. Yu, Z. Shui, K. Liu, Y. Feng, S. Wang, K. Li, J. Tan, Y. He, A new development of eco-friendly Ultra-High performance concrete (UHPC): towards efficient steel slag application and multi-objective optimization, *Constr. Build. Mater.* 306 (2021) 124913, <https://doi.org/10.1016/j.conbuildmat.2021.124913>.
- [7] Z. Liu, H. Zeng, F. Wang, Development of high performance carbonatable concrete for steel slag valorization, *Constr. Build. Mater.* 291 (2021) 123317, <https://doi.org/10.1016/j.conbuildmat.2021.123317>.
- [8] V.S. Devi, B.K. Gnanavel, Properties of concrete manufactured using steel slag, *Procedia Eng.* 97 (2014) 95–104, <https://doi.org/10.1016/j.proeng.2014.12.229>.
- [9] M. Maslehuddin, A.M. Sharif, M. Shameem, M. Ibrahim, M.S. Barry, Comparison of properties of steel slag and crushed limestone aggregate concretes, *Constr. Build. Mater.* 17 (2) (2003) 105–112, [https://doi.org/10.1016/S0950-0618\(02\)00095-8](https://doi.org/10.1016/S0950-0618(02)00095-8).

- [10] N. Palankar, A.U. Ravi Shankar, B.M. Mithun, Durability studies on eco-friendly concrete mixes incorporating steel slag as coarse aggregates, *J. Clean. Prod.* 129 (2016) 437–448, <https://doi.org/10.1016/j.jclepro.2016.04.033>.
- [11] S. Saxena, A.R. Tembhurkar, Impact of use of steel slag as coarse aggregate and wastewater on fresh and hardened properties of concrete, *Constr. Build. Mater.* 165 (2018) 126–137, <https://doi.org/10.1016/j.conbuildmat.2018.01.030>.
- [12] Y. Guo, J. Xie, J. Zhao, K. Zuo, Utilization of unprocessed steel slag as fine aggregate in normal- and high-strength concrete, *Constr. Build. Mater.* 204 (2019) 41–49, <https://doi.org/10.1016/j.conbuildmat.2019.01.178>.
- [13] H. Qasrawi, F. Shalabi, I. Asi, Use of low CaO unprocessed steel slag in concrete as fine aggregate, *Constr. Build. Mater.* 23 (2) (2009) 1118–1125, <https://doi.org/10.1016/j.conbuildmat.2008.06.003>.
- [14] M.H. Lai, J. Zou, B. Yao, J.C.M. Ho, X. Zhuang, Q. Wang, Improving mechanical behavior and microstructure of concrete by using BOF steel slag aggregate, *Constr. Build. Mater.* 277 (2021) 122269, <https://doi.org/10.1016/j.conbuildmat.2021.122269>.
- [15] Y.L. Wei, C.Y. Lin, S.H. Cheng, H.P. Wang, Recycling steel-manufacturing slag and harbor sediment into construction materials, *J. Hazard. Mater.* 265 (2014) 253–260, <https://doi.org/10.1016/j.jhazmat.2013.11.049>.
- [16] G. Liu, K. Schollbach, P. Li, H.J.H. Brouwers, Valorization of converter steel slag into eco-friendly ultra-high performance concrete by ambient CO<sub>2</sub> pre-treatment, *Constr. Build. Mater.* 280 (2021) 122580, <https://doi.org/10.1016/j.conbuildmat.2021.122580>.
- [17] S. Li, G. Liu, Q. Yu, The role of carbonated steel slag on mechanical performance of ultra-high performance concrete containing coarse aggregates, *Constr. Build. Mater.* 307 (2021) 124903, <https://doi.org/10.1016/j.conbuildmat.2021.124903>.
- [18] K. Sun, X. Peng, S.H. Chu, S. Wang, L.u. Zeng, G. Ji, Utilization of BOF steel slag aggregate in metakaolin-based geopolymer, *Constr. Build. Mater.* 300 (2021) 124024, <https://doi.org/10.1016/j.conbuildmat.2021.124024>.
- [19] M. Papachristoforou, E.K. Anastasiou, I. Papayianni, Durability of steel fiber reinforced concrete with coarse steel slag aggregates including performance at elevated temperatures, *Constr. Build. Mater.* 262 (2020) 120569, <https://doi.org/10.1016/j.conbuildmat.2020.120569>.
- [20] H.D. Andrade, J.M.F. de Carvalho, L.C.B. Costa, F.P.d.F. Elói, K.D.d.C. e Silva, R.A. F. Peixoto, Mechanical performance and resistance to carbonation of steel slag reinforced concrete, *Constr. Build. Mater.* 298 (2021) 123910, <https://doi.org/10.1016/j.conbuildmat.2021.123910>.
- [21] R. Malathy, M. Arivoli, I.-M. Chung, M. Prabakaran, Effect of surface-treated energy optimized furnace steel slag as coarse aggregate in the performance of concrete under corrosive environment, *Constr. Build. Mater.* 284 (2021) 122840, <https://doi.org/10.1016/j.conbuildmat.2021.122840>.
- [22] J. Baalamurugan, V.G. Kumar, S. Chandrasekaran, S. Balasundar, B. Venkatraman, R. Padmapriya, V.K.B. Raja, Utilization of induction furnace steel slag in concrete as coarse aggregate for gamma radiation shielding, *J. Hazard. Mater.* 369 (2019) 561–568, <https://doi.org/10.1016/j.jhazmat.2019.02.064>.
- [23] Baalamurugan et al., (2021). J.Baalamurugan, V. G.Kumar, S.Chandrasekaran, S. Balasundar, B.Venkatraman, R.Padmapriya, V.K. B. Raja, Recycling of steel slag aggregates for the development of high density concrete: Alternative & environment-friendly radiation shielding composite. *Compos. B Eng.* 216(2021) 108885. <https://doi.org/10.1016/j.compositesb.2021.108885>.
- [24] A.S. Brand, J.R. Roesler, Steel furnace slag aggregate expansion and hardened concrete properties, *Cem. Concr. Compos.* 60 (2015) 1–9, <https://doi.org/10.1016/j.cemconcomp.2015.04.006>.
- [25] Q. Wang, D. Wang, S. Zhuang, The soundness of steel slag with different free CaO and MgO contents, *Constr. Build. Mater.* 151 (2017) 138–146, <https://doi.org/10.1016/j.conbuildmat.2017.06.077>.
- [26] Q. Wang, P. Yan, Hydration properties of basic oxygen furnace steel slag, *Constr. Build. Mater.* 24 (7) (2010) 1134–1140, <https://doi.org/10.1016/j.conbuildmat.2009.12.028>.
- [27] Q. Wang, P. Yan, J. Yang, B. Zhang, Influence of steel slag on mechanical properties and durability of concrete, *Constr. Build. Mater.* 47 (2013) 1414–1420, <https://doi.org/10.1016/j.conbuildmat.2013.06.044>.
- [28] W.T. Kuo, C.Y. Shu, Effect of particle size and curing temperature on expansion reaction in electric arc furnace oxidizing slag aggregate concrete, *Constr. Build. Mater.* 94 (2015) 488–493, <https://doi.org/10.1016/j.conbuildmat.2015.07.019>.
- [29] J. Wang, P. Feng, T. Hao, Q. Yue, Axial compressive behavior of seawater coral aggregate concrete-filled FRP tubes, *Constr. Build. Mater.* 147 (2017) 272–285, <https://doi.org/10.1016/j.conbuildmat.2017.04.169>.
- [30] T. Liu, X. Liu, P. Feng, A comprehensive review on mechanical properties of pultruded FRP composites subjected to long-term environmental effects, *Compos. B Eng.* 191 (2020) 107958, <https://doi.org/10.1016/j.compositesb.2020.107958>.
- [31] S. Cheng, P. Feng, Y.u. Bai, L.P. Ye, Load-strain model for steel-concrete-FRP-concrete columns in axial compression, *J. Compos. Constr.* 20 (5) (2016) 04016017, [https://doi.org/10.1061/\(ASCE\)CC.1943-5614.0000664](https://doi.org/10.1061/(ASCE)CC.1943-5614.0000664).
- [32] A. Mirmiran, M. Shahawy, M. Samaan, H.E. Echary, J.C. Mastrapa, O. Pico, Effect of column parameters on FRP-confined concrete, *J. Compos. Constr.* 2 (4) (1998) 175–185.
- [33] W. Zhou, P. Feng, H. Lin, Constitutive relations of coral aggregate concrete under uniaxial and triaxial compression, *Constr. Build. Mater.* 251 (2020) 118957, <https://doi.org/10.1016/j.conbuildmat.2020.118957>.
- [34] Z. Dang, P. Feng, J.-Q. Yang, Q. Zhang, Axial compressive behavior of engineered cementitious composite confined by fiber-reinforced polymer, *Compos. Struct.* 243 (2020) 112191, <https://doi.org/10.1016/j.compstruct.2020.112191>.
- [35] P. Feng, S. Cheng, Y. Bai, L. Ye, Mechanical behavior of concrete-filled square steel tube with FRP-confined concrete core subjected to axial compression, *Compos. Struct.* 123 (2015) 312–324, <https://doi.org/10.1016/j.compstruct.2014.12.053>.
- [36] J.-Q. Yang, P. Feng, Analysis-oriented models for FRP-confined concrete: 3D interpretation and general methodology, *Eng. Struct.* 216 (2020) 110749, <https://doi.org/10.1016/j.engstruct.2020.110749>.
- [37] J.-Q. Yang, P. Feng, Analysis-oriented model for FRP confined high-strength concrete: 3D interpretation of path dependency, *Compos. Struct.* 278 (2021) 114695, <https://doi.org/10.1016/j.compstruct.2021.114695>.
- [38] Z. Wang, P. Feng, Y.i. Zhao, T. Yu, FRP-confined concrete core-encased rebar for RC columns: Concept and axial compressive behavior, *Compos. Struct.* 222 (2019) 110915, <https://doi.org/10.1016/j.compstruct.2019.110915>.
- [39] P. Feng, X. Meng, H. Zhang, Mechanical behavior of FRP sheets reinforced 3D elements printed with cementitious materials, *Compos. Struct.* 134 (2015) 331–342, <https://doi.org/10.1016/j.compstruct.2015.08.079>.
- [40] J.G. Teng, T. Yu, Y.L. Wong, S.L. Dong, Hybrid FRP-concrete-steel tubular columns: Concept and behavior, *Constr. Build. Mater.* 21 (4) (2007) 846–854, <https://doi.org/10.1016/j.conbuildmat.2006.06.017>.
- [41] L. Huang, T. Yu, S.S. Zhang, Z.Y. Wang, FRP-confined concrete-encased cross-shaped steel columns: Concept and behaviour, *Eng. Struct.* 152 (2017) 348–358, <https://doi.org/10.1016/j.engstruct.2017.09.011>.
- [42] L. Huang, S.S. Zhang, T. Yu, Z.Y. Wang, Compressive behaviour of large rupture strain FRP-confined concrete-encased steel columns, *Constr. Build. Mater.* 183 (2018) 513–522, <https://doi.org/10.1016/j.conbuildmat.2018.06.074>.
- [43] J.S. Park, S.S. Lee, J.H. Nam, I.K. Kang, D.J. An, S.J. Yoon, Load carrying capacity of hybrid FRP-concrete composite pile, *Adv. Mater. Res.* 250–253 (2011) 1165–1172, <https://doi.org/10.4028/www.scientific.net/amr.250-253.1165>.
- [44] T. Vincent, T. Ozbakkaloglu, Influence of shrinkage on compressive behavior of concrete-filled FRP tubes: an experimental study on interface gap effect, *Constr. Build. Mater.* 75 (2015) 144–156, <https://doi.org/10.1016/j.conbuildmat.2014.10.038>.
- [45] P. Feng, J. Yang, Z. Li, Hybrid members incorporating FRP confined concrete core, in: Seventh Asia-Pacific Conference on FRP in Structures (APPIS 2019), Surfers Paradise, Gold Coast, Australia, 2019.
- [46] Chinese National Standard, Standard for Test Method of Mechanical Properties on Ordinary Concrete, GB/T 50081–2002, China Architecture & Building Press, Beijing, China, 2002.
- [47] S.H. Chu, Effect of paste volume on fresh and hardened properties of concrete, *Constr. Build. Mater.* 218 (2019) 284–294, <https://doi.org/10.1016/j.conbuildmat.2019.05.131>.
- [48] W. Ding, F.G. Leng, Specification for mix proportion design of ordinary concrete, JGJ55-2011, China Architecture & Building Press, Beijing, China, 2011.
- [49] B.V. Farahani, F. Barros, P.J. Sousa, P.P. Cacciari, P.J. Tavares, M.M. Futai, P. Moreira, A coupled 3D laser scanning and digital image correlation system for geometry acquisition and deformation monitoring of a railway tunnel, *Tunn. Undergr. Space Technol.* 91 (2019) 102995, <https://doi.org/10.1016/j.tust.2019.102995>.
- [50] P. Feng, Y. Zou, L. Hu, T. Liu, Use of 3D laser scanning on evaluating reduction of initial geometric imperfection of steel column with pre-stressed CFRP, *Eng. Struct.* 198 (2019) 109527, <https://doi.org/10.1016/j.engstruct.2019.109527>.
- [51] J. Liu, Q. Zhang, J. Wu, Y. Zhao, Dimensional accuracy and structural performance assessment of spatial structure components using 3D laser scanning, *Autom. Constr.* 96 (2018) 324–336, <https://doi.org/10.1016/j.autcon.2018.09.026>.
- [52] M.K. Kim, J.C.P. Cheng, H. Sohn, C.C. Chang, A framework for dimensional and surface quality assessment of precast concrete elements using BIM and 3D laser scanning, *Autom. Constr.* 49 (2015) 225–238, <https://doi.org/10.1016/j.autcon.2014.07.010>.
- [53] M.K. Kim, Q. Wang, S. Yoon, H. Sohn, A mirror-aided laser scanning system for geometric quality inspection of side surfaces of precast concrete elements, *Measurement* 141 (2019) 420–428, <https://doi.org/10.1016/j.measurement.2019.04.060>.
- [54] L. Lam, J.G. Teng, Design-oriented stress-strain model for FRP-confined concrete, *Constr. Build. Mater.* 17 (6-7) (2003) 471–489.
- [55] J.G. Teng, T. Jiang, L. Lam, Y.Z. Luo, Refinement of a design-oriented stress-strain model for FRP-confined concrete, *J. Compos. Constr.* 13 (4) (2009) 269–278.